

Journal of Materials Chemistry A

Accepted Manuscript

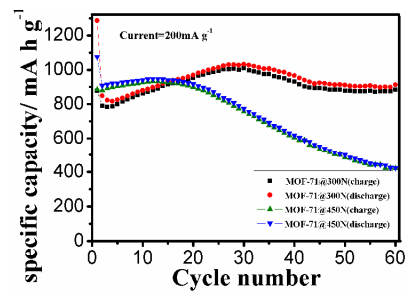


This is an *Accepted Manuscript*, which has been through the Royal Society of Chemistry peer review process and has been accepted for publication.

Accepted Manuscripts are published online shortly after acceptance, before technical editing, formatting and proof reading. Using this free service, authors can make their results available to the community, in citable form, before we publish the edited article. We will replace this *Accepted Manuscript* with the edited and formatted *Advance Article* as soon as it is available.

You can find more information about *Accepted Manuscripts* in the [Information for Authors](#).

Please note that technical editing may introduce minor changes to the text and/or graphics, which may alter content. The journal's standard [Terms & Conditions](#) and the [Ethical guidelines](#) still apply. In no event shall the Royal Society of Chemistry be held responsible for any errors or omissions in this *Accepted Manuscript* or any consequences arising from the use of any information it contains.



Mesoporous nanostructured Co₃O₄, prepared through direct pyrolysis of MOF-71 template at a relatively low temperature, shows good electrochemical performance.

Cite this: DOI: 10.1039/c0xx00000x

www.rsc.org/xxxxxx

ARTICLE TYPE

Mesoporous nanostructured Co_3O_4 derived from MOF template: a high-performance anode material for lithium-ion batteries†

Chao Li,^a Taiqiang Chen,^a Weijing Xu,^a Xiaobing Lou,^a Likun Pan,^a Qun Chen^a and Bingwen Hu^{*a}

Received (in XXX, XXX) Xth XXXXXXXXXX 20XX, Accepted Xth XXXXXXXXXX 20XX

DOI: 10.1039/b000000x

Mesoporous nanostructured Co_3O_4 was prepared through direct pyrolysis of Co-based metal organic framework (MOF) template at a relatively low temperature rather than high temperature. When tested as anode material for lithium-ion batteries (LIBs), this porous Co_3O_4 exhibits greatly enhanced performance of lithium storage. The capacity of the porous Co_3O_4 retained 913 mA h g^{-1} after 60 cycles at a current rate of 200 mA g^{-1} . Excellent rate capability was also achieved. We also found out that the Co_3O_4 prepared from MOF template at a relatively low temperature has better electrochemical performance than that prepared at high temperature.

Introduction

For several decades, room-temperature rechargeable lithium-ion batteries (LIBs) have been employed for large-scale applications in various fields, such as hybrid electric vehicles (HEVs), electrical energy storage (EES), medical and military devices, and smart grid applications.¹⁻³ In order to meet the increasing requirements of aforementioned applications, a significant research attention has been turned to design new sustainable electrode materials with high cycling performance, large energy and power densities, low cost, manufacturing ease and environmentally benignity for state-of-the-art LIBs.^{4,5} Among these available anode materials, tricobalt tetraoxygen (Co_3O_4) has garnered considerable interest as a promising candidate to replace currently commercial graphite anode for next generation LIBs owing to its high theoretical capacity of 890 mA h g^{-1} , which is more than twice that of graphite (372 mA h g^{-1}).⁶⁻⁸ However, upon charge-discharge processes, Co_3O_4 suffers from large volume expansion/contraction and subsequently electrode pulverization which may lead to a large reversible capacity fading and poor cycling performance.⁹⁻¹¹ Thus, an effective architecture must be designed to maintain the integrity of the electrode material and prevent its disintegration. For this aim, sophisticated nano- and microstructures, including nanowires,¹² nanobelts,¹³ nanotubes,¹⁴ nanosheets,¹⁵ nanorods¹⁶ and porous hollow spheres¹⁷ have been fabricated to improve the electrode performance. To date, the most popular method for the synthesis of advanced Co_3O_4 nano/microstructures is templating approach. These templates including inorganic clusters, Co-based coordination polymer, which were prepared first and then convert into specially structured Co_3O_4 via thermal treatment.¹²⁻¹⁴

Recently, metal organic frameworks (MOFs) have been discovered as a promising class of micro-porous materials, which possess high specific surface area and ultrahigh porosity because of the enriched organic ligands and metal ions in MOFs

structure.¹⁸⁻²² Great efforts have been devoted to preparing new MOFs and exploiting their applications, including gas storage,²³ selective separation,²⁴ catalysis,²⁵ electron²⁶ and proton²⁷ conductivity. In addition, MOFs can be employed as sacrificial templates to convert into functional nanomaterials for LIBs.²⁸⁻³³ For instance, spindle-like mesoporous $\alpha\text{-Fe}_2\text{O}_3$ has been prepared from MIL-88-Fe template for high-rate LIBs.²⁹ By using Co-based zeolitic imidazolate framework (ZIF-67) as template, ball-in-dodecahedron Co_3O_4 has been prepared after one-step calcination. When tested as anode material for LIBs, this ball-in-dodecahedron Co_3O_4 shows high reversible capacity and excellent cycling stability.³⁴ As compared to other templates, MOFs offer unique advantages due to their high porosity, large surface area and easily removable features. Moreover, pyrolyzing MOFs can effectively reduce surface areas, expand their pores to mesopores and boost their conductivity while maintaining the open diffusion channels.²⁸

Herein, we report a facile and scalable method to obtain mesoporous nanostructured Co_3O_4 by using [Co(bdc)(DMF)] (MOF-71, bdc = 1,4-benzenedicarboxylate, DMF = N,N-dimethylformamide) as template. The as-synthesized mesoporous Co_3O_4 has high specific surface area, reasonable pore volume and small crystallite size. More importantly, when applied as anode material, the as-prepared mesoporous Co_3O_4 exhibits significantly improved electrochemical performance with a high reversible capacity of 913 mA h g^{-1} after 60 cycles at a current rate of 200 mA g^{-1} . As far as we know, this is one of the best anode materials of Co_3O_4 category with such an incredible cycling performance.

Results and discussion

2.1 Material characterization

MOF-71 is one of the most well-studied and easily available Co-based MOFs.³⁵ The structure of the framework consists of

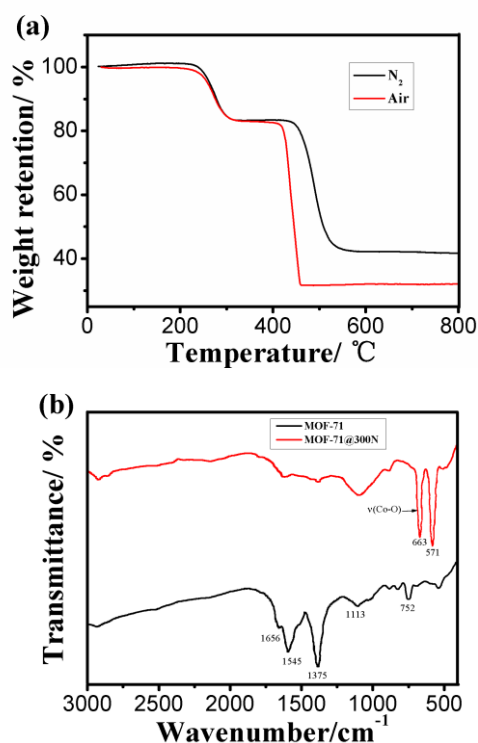


Fig. 1 (a) TG curves of Co-MOF-71 under air and nitrogen atmosphere. (b) FTIR spectra of MOF-71 and MOF-71@300N. (e.g. 300N denotes a sample calcinated at 300 °C under air atmosphere)

infinite chains of corner-sharing CoO_6 octahedra, with each chain linked to four parallel running chains via the bdc linkers.³⁶ The thermal behavior of MOF-71 was investigated through thermogravimetric (TG) analysis (Fig. 1a), which indicated that MOF-71 underwent a drastic weight loss between 400 °C and 450 °C and remained at ~32 % of its original weight when subjected to heat treatment under air atmosphere. As the temperature continued to rise, no weight loss was observed, indicating the complete decomposition of the organic ligands in MOF-71 and the simultaneous formation of Co_3O_4 at temperatures above 450 °C. However, in this work, we treated the as-prepared Co-MOF-71 at a relatively low temperature (300 °C) for a relatively long reaction time (12 h), which is different from previous works.²⁹⁻³³ The Co_3O_4 sample calcinated at 450 °C for 1.5 h (similar to previous works) was also prepared for the purpose of comparison. For ease of description, we call them MOF-71@300N and MOF-71@450N for the MOF-71 treated at 300 °C or 450 °C, respectively. Fig. 1b presents the FTIR spectrum of MOF-71 and the MOF-71@300N. The specific peaks around 570 and 660 cm^{-1} of MOF-71@300N correspond to the Co_3O_4 adsorption bands, which confirmed that the MOF-71 transformed to pure Co_3O_4 after calcination at 300 °C for 12 h. MOF-71@450N shows similar specific peaks as MOF-71@300N, confirming the formation of pure Co_3O_4 , too (Fig. S2). In addition, the obtained MOF-71@300N and MOF-71@450N materials exhibit no weight loss upon TG analysis (Fig. S3 and S4), excluding the possibility that some undecomposed carbon residues may be left in the final product.

The interior structure of the as-prepared Co_3O_4 materials were investigated by transmission electron microscopy (TEM) and

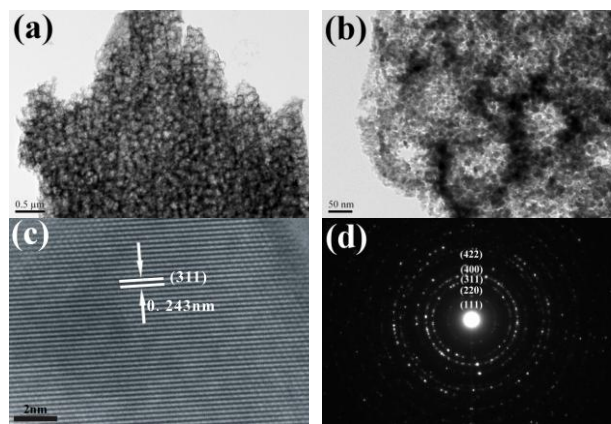


Fig. 2 (a) Low-magnification TEM image of the porous MOF-71@300N materials. (b) High-magnification TEM image of MOF-71@300N materials. (c) Lattice resolved TEM image of MOF-71@300N materials, from which the lattice spacing of (311) plane was determined. (d) The SAED patterns taken from (c), from which the polycrystalline nature of MOF-71@300N was determined.

high-resolution transmission electron microscopy (HRTEM). Fig. 2a shows a low magnification TEM image of MOF-71@300N, from which we can see that Co_3O_4 have agglomerated nanostructure with coarse surface. The magnified TEM image in Fig. 2b further confirms that the Co_3O_4 materials have an integrated porous nanoarchitecture which contains inner nanosize pores. The porous structure was composed by Co_3O_4 primary particles of several to dozens nanometers in size and those primary particles were embedded tightly into a ruleless porous matrix. The lattice resolved HRTEM image presented in Fig. 2c illustrates the interplanar distances of the (311) crystal plane (2.43 Å). In addition, the corresponding selected area electron diffraction (SAED) pattern (Fig. 2d) shows a polycrystalline nature of MOF-71@300N, indicating that the porous Co_3O_4 structure is randomly oriented. The TEM and HRTEM of MOF-71@450N are shown in Fig. S5, in which a more uniform architecture were illustrated. The size of Co_3O_4 primary particles of MOF-71@450N are larger and more regular compared with those of MOF-71@300N. It should be mentioned that MOF-71@300N and MOF-71@450N have different morphologies compared with the MOF-71 (Fig. S1b and c).

The Powder X-ray diffraction (PXRD) patterns of the two products after the one-step calcination of Co-MOF-71 are shown in Fig. 3a. All reflections in the two samples are in good agreement with a pure Co_3O_4 spinel phase with a face-centered cubic lattice (JCPDS Card no. 42-1467, cell parameter $a=8.0837$ Å). No residues or contaminants were present, indicating the high purity of the samples. The intensive and sharp peaks of MOF-71@450N indicate a good crystallization. MOF-71@300N shows peaks located at nearly the same angles corresponding to those of MOF-71@450N, however, the peaks become broader and weaker due to the reduced crystallite size, suggesting a polycrystalline structure, which is consistent with the SAED analysis (Fig. 2d). The average crystallite sizes of MOF-71@300N and MOF-71@450N calculated from the XRD data using the Scherrer equation ($D = 0.89\lambda / B \cos\theta$) were estimated to be 14 nm and 29 nm, respectively.

To gain insight into the porous structures of these materials, nitrogen adsorption-desorption isotherms at 77 K were measured,

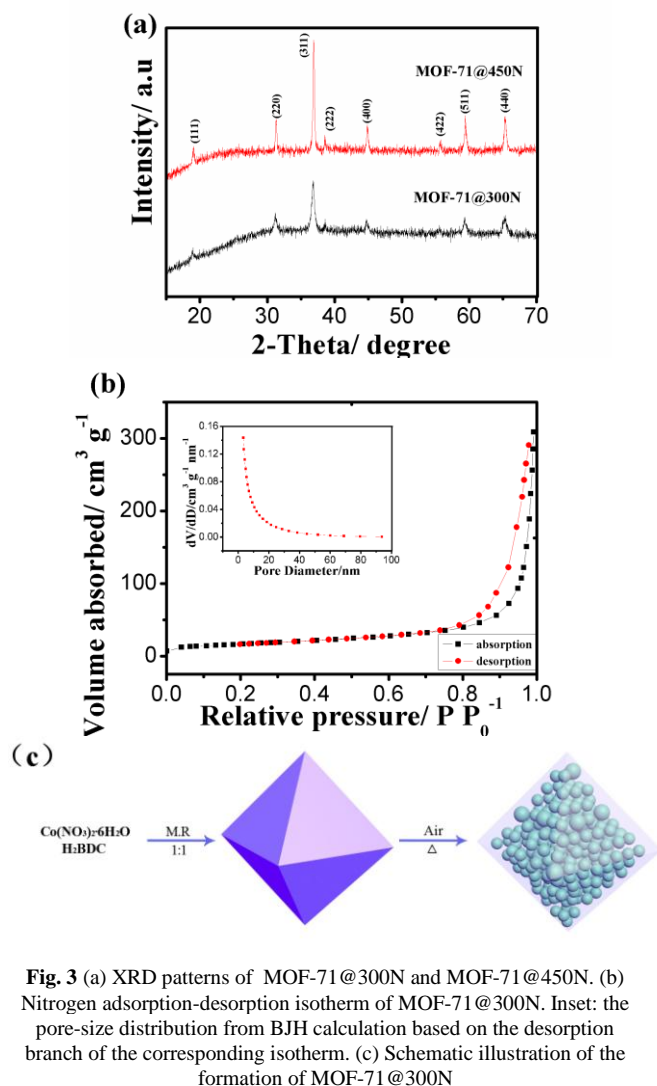


Fig. 3 (a) XRD patterns of MOF-71@300N and MOF-71@450N. (b) Nitrogen adsorption-desorption isotherm of MOF-71@300N. Inset: the pore-size distribution from BJH calculation based on the desorption branch of the corresponding isotherm. (c) Schematic illustration of the formation of MOF-71@300N

after heating the sample under vacuum at 300 °C for 6 h. As shown in Fig. 3b, after pyrolyzing MOF-71 in air, MOF-71@300N shows typical type IV curves with hysteresis loops, indicating the mesoporous feature. It is found that porous Co₃O₄ have a broad pore-size distribution and a first-rate BET specific surface area of 59.0 m² g⁻¹ (Table S1), which is higher than that of most reported Co₃O₄ nanostructures.^{34,37} In contrast, the BET specific surface area of MOF-71@450N is 16.2 m² g⁻¹, much smaller than the former. Moreover, the pore volume (0.4483 cm³ g⁻¹) and mean pore diameter (30.389 nm) of MOF-71@300N are larger than MOF-71@450N (0.0619 cm³ g⁻¹ and 15.253 nm, respectively), which can provide more buffer space for the volume expansion of Co₃O₄ and better Li-ion transfer path during charge-discharge process. Observations of the nitrogen sorption are in good agreement with the previous microscopy observations in Fig. 2 and Fig. S5. A schematic is shown in Fig. 3c to illustrate the formation of MOF-71@300N. The formation of pores in Co₃O₄ nanoparticles originated from gas evolution due to thermal decomposition of Co-MOF template. Compared to the previously reported route which pyrolyzing the MOF template at higher temperature,³⁸ our approach in this paper can obtain the Co₃O₄ nanoparticles with smaller crystallite size and mesoporous nature.

Such a unique porous Co₃O₄ structure with small crystallite size and large pore volume can provide not only fast electronic and ionic conducting channels but also adequate buffer space for the volume expansion of Co₃O₄ during cycling process. Therefore, the as-prepared mesoporous Co₃O₄ provides critical features for high-performance electrodes: short diffusion length for Li⁺, fast electron and Li⁺ transportation, large surface reaction sites, low surface energy, and excellent endurance for internal stress.

2.2 Electrochemical performance

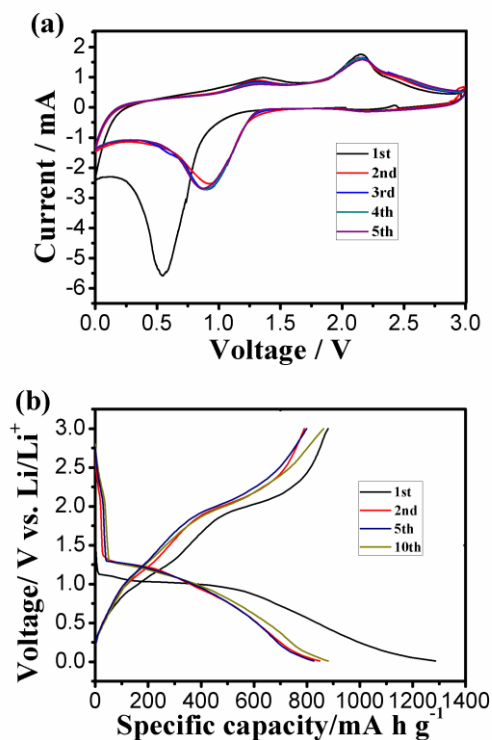


Fig. 4 (a) Cyclic voltammograms for the first five cycles of MOF-71@300N electrode. (b) Representative charge-discharge voltage profiles of MOF-71@300N electrode at a current density of 200 mA g⁻¹.

The electrochemical characteristics of the mesoporous nanostructured Co₃O₄ materials for lithium storage were evaluated by cyclic voltammetry (CV) and galvanostatic charge/discharge testing. Fig. 4a presents the first five consecutive CV curves of the MOF-71@300N electrode at a scan rate of 0.5 mV s⁻¹. The reversible reaction of Co₃O₄ with lithium could be described by the following electrochemical conversion reactions:³⁹

- 1) $\text{Co}_3\text{O}_4 + 8\text{Li}^+ + 8\text{e}^- \rightarrow 3\text{Co} + 4\text{Li}_2\text{O}$ (First lithiation)
- 2) $\text{Co} + \text{Li}_2\text{O} \rightarrow \text{CoO} + 2\text{Li}^+ + 2\text{e}^-$ (Subsequent delithiation/lithiation)

In the first cycle, one cathodic peak at 0.56 V can be attributed to the electrochemical reduction reaction of Co₃O₄ to metallic cobalt and the irreversible decomposition of the solvent in the electrolyte to form the solid-electrolyte interface (SEI).⁴⁰ One prominent anodic peak is observed at 2.22 V accompanying with a slight peak at 1.35 V, which could be attributed to the multistep oxidation reactions of Co⁰ to CoO. The peak of 1.35V

could be possibly ascribed to CoO_x ($0 < x < 1$), an intermediate state between Co and CoO. Compared to the first cycle, a significant decrease of the cathodic peak's intensity and a shift of the potential to the positive direction (~ 0.85 V) appeared in the subsequent cycles, while the main anodic peak at ~ 2.2 V showed pinging modification. The peak intensities and integral areas were nearly identical, suggesting the good reversibility of lithium insertion and extraction reactions in the subsequent cycles.

Fig. 4b shows the representative discharge-charge voltage profiles of MOF-71@300N within a cutoff voltage window of 0.001–3.0 V vs. Li^+/Li at a constant current density of 200 mA g^{-1} , which is consistent with typical discharge-charge voltage profiles of porous Co_3O_4 .⁸ The initial discharge and charge capacities were found to be 1286.1 and $879.5 \text{ mA h g}^{-1}$, respectively. The low Coulombic efficiency of 68% may be caused by the irreversible capacity loss, including decomposition of electrolyte to form SEI layers and interfacial lithium storage.^{41,42} Moreover, it is noteworthy to mention that MOF-71@300N has a larger BET surface area compared with MOF-71@450N, so more robust SEI layer can be formed on the surface of MOF-71@300N, resulting in its relatively lower initial Coulombic efficiency compared to MOF-71@450N (82.34%). The second discharge curve is different in shape from the first discharge curve and the plateau region is slightly higher, whereas the two charge curves are analogous. These results are also in agreement with the CV curves shown in Fig. 4a. Compared with the discharge-charge voltage profiles of MOF-71@450N (Fig. S6), the plateaus become less prominent with more sloping characteristic because of smaller crystallite size and higher surface area of MOF-71@300N that create more active sites for Li^+ reaction.

The cycling performances of MOF-71@300N and MOF-71@450N are shown in Fig. 5a at a current density of 200 mA g^{-1} between 0.001V and 3V. In the initial 30 cycles, the capacities of MOF-71@300N electrode were gradually increasing and achieved a maximum discharge capacity and charge capacity of 1031.8, 1008 mA h g^{-1} , respectively at the 30th cycle. After 60 cycles, MOF-71@300N still exhibited a very high discharge capacity of 913 mA h g^{-1} , still higher than the theoretical capacity (890 mA h g^{-1}). Furthermore, its Coulombic efficiency was maintained at $\sim 97\%$ (Fig. 5b) after the 3rd cycle. A nearly 100% Coulombic efficiency suggests the stability of the SEI layer.⁴³ As a comparison, MOF-71@450N shown a quickly decrease of capacity to less than 450 mA h g^{-1} after 60 cycles, although the reversible capacities of the initial 15 cycles were better than the former. Fig. S8 shows the Nyquist plots of MOF-71@300N and MOF-71@450N at the 30th cycle. It is obviously shown that the impedance associated charge-transfer resistance in MOF-71@300N is lower than that of MOF-71@450N, demonstrating the better conductive capability of the MOF-71@300N electrode. The ultrahigh capacity retention of MOF-71@300N after 60 cycles could be possibly attributed to the reversible formation/dissolution of polymeric gel-like layer resulting from kinetically activated electrolyte degradation or further lithium storage as a result of interface reaction in the process of activation and stabilization of the electrode.^{30,37,44} Such high capacity retention of Co_3O_4 at a current rate of 200 mA g^{-1} is few reported.

Compared with other Co_3O_4 electrodes tested under similar conditions ($\sim 200 \text{ mA g}^{-1}$, Table S2), our mesoporous MOF-71@300N reveals greatly enhanced Li storage properties with higher reversible capacity. Moreover, in comparison with other MOFs-derived Co_3O_4 materials, our MOF-71@300N shows competitive reversible capacity while using a more facile method.^{34,38,47}

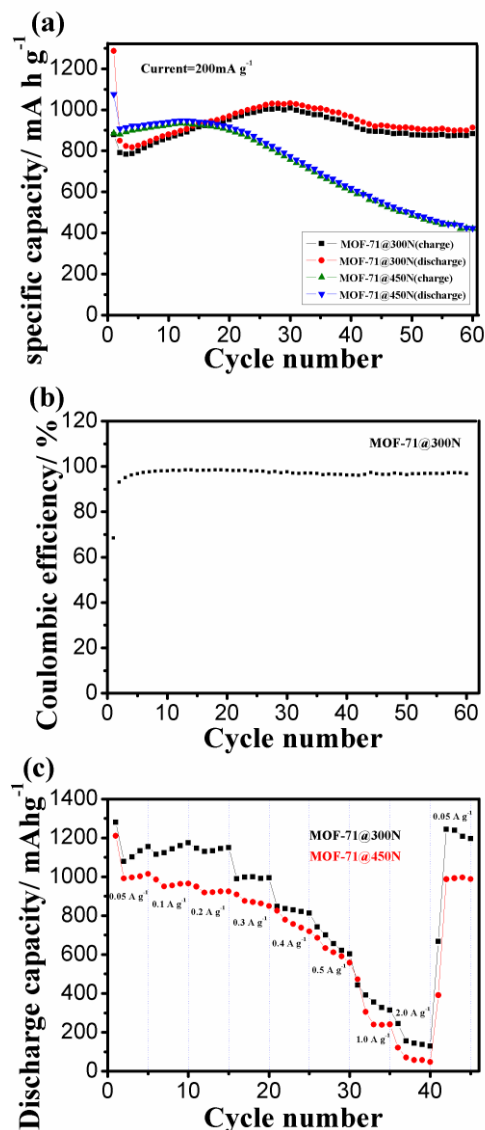


Fig. 5 (a) Cyclic performances of MOF-71@300N and MOF-71@450N electrodes at a current density of 200 mA g^{-1} . (b) Coulombic efficiencies of MOF-71@300N electrode when cycling at 200 mA g^{-1} (c) Rate performances of MOF-71@300N and MOF-71@450N electrodes.

The rate performances of MOF-71@300N and MOF-71@450N are evaluated at various current densities from 50 to 2000 mA g^{-1} , as presented in Fig. 5c. It is found that the discharge capacity of MOF-71@300N remains at 1146, 742.5, $442.1 \text{ mA h g}^{-1}$ at rates of 200, 500, and 1000 mA g^{-1} , respectively, showing better performance than those of MOF-71@450N ($949.2, 685.6, 305 \text{ mA h g}^{-1}$ at rates of 200, 500, and 1000 mA g^{-1}). After enduring various charge-discharge rates, the MOF-71@300N anode resumes its capacity of about 1200 mA h g^{-1} with the rate back to 50 mA g^{-1} and maintains this value

without any apparent decay. The slight increase of the discharge capacity may attribute to partial Li^+ remaining in the electrodes during charging with higher current densities.^{28,48}

Such superior cycle and rate performance of MOF-71@300N anode could probably be attributed to the unique porous structure verified by TEM and BET measurement. Firstly, the small Co_3O_4 nanoparticles can decrease the diffusion length of Li ions within the particles. Secondly, the void space of MOF-71@300N can effectively buffer the strong volumetric expansion seen during charge–discharge cycling, hence alleviate the pulverization of the electrode and improve the cycling stability. To verify this hypothesis, the electrode at the fully lithiated state after 30 cycles was separated from the LIB, then it was washed with a large amount of EtOH and fully dried in a vacuum oven for more than 24 h, and then it was characterized by TEM. As shown in Fig. S10, the electrode material maintains small crystallite size and large pore volume after 30 cycles; so it reveals the excellent structural stability of MOF-71@300N, which is one of the main reasons for superior performance of the porous Co_3O_4 materials. Thirdly, the porous structure ensures efficient electrolyte penetration between the Co_3O_4 particles and enhances the contact area between the electrode and electrolyte. Finally, a robust SEI layer can be formed on the surface of MOF-71@300N electrode due to the large specific surface area buffering the volumetric expansion and the crack of the SEI layer which is essential to preventing particles from sintering into larger particles and realizing higher performance for LIBs.

Conclusions

In summary, mesoporous nanostructured Co_3O_4 has been synthesized by a simple and scalable strategy, which involves the preparation of a Co–based MOF template via a hydrothermal method and subsequent thermal decomposition of the MOF template at a relatively low temperature rather than high temperature. In view of their unique structural advantages, these as-synthesized mesoporous nanostructured Co_3O_4 evaluated anode exhibit excellent performance in LIBs with very stable cycling performance and good rate capability. This work may provide a novel way for fabricating mesoporous nanostructured metal oxides for lithium-ion batteries.

Experimental details

Synthesis of Co-MOF-71

The cobalt-based Co-MOF-71, $[\text{Co}(\text{bdc})(\text{DMF})]$, was synthesized following a previously reported method.³⁵ Typically, $\text{Co}(\text{NO}_3)_2 \cdot 6\text{H}_2\text{O}$ (0.75 g) and terephthalic acid (0.428 g) were dissolved in 48 mL DMF and 12 mL absolute EtOH. After thoroughly mixing, the solution was transferred into a 100 mL Teflon-lined stainless steel autoclave and placed in an oven at 100 °C for 12 h. After the autoclave was cooled down naturally to room temperature in a fumehood, the resultant crystal was collected by centrifugation, washed thoroughly with DMF and EtOH. Finally, the purple powder of Co-MOF-71 was obtained after drying in a vacuum oven at 110 °C for 12 h.

Preparation of porous nanostructured Co_3O_4

MOF-71@300N was prepared through a one-step calcination of

Co-MOF-71 in a furnace under a flow of air. The temperature was raised from room temperature to 300 °C at a ramping rate of 10 °C min^{-1} , and then stabilized at 300 °C for 12 h. Finally, the product was taken out and it was found that the color changed from purple to black. MOF-71@450N was prepared through a similar process, only the calcinating temperature (450 °C) and stability time (1.5 h) were different.

Characterization of materials

The crystal phase of the as-prepared materials were characterized by X-Ray diffraction (XRD, Holland Panalytical PRO PW3040/60) with Cu-K α radiation ($V = 30$ kV, $I = 25$ mA, $\lambda = 1.5418$ Å). Internal structures of the samples were studied using transmission electron microscope (TEM, JEOL JEM-2100F). Thermogravimetric analysis (TGA) was carried out by using STA 449 F3 Jupiter® simultaneous thermo-analyzer at a ramping rate 10 °C/min from room temperature to 800 °C. Fourier transform infrared spectroscopy (FTIR) was recorded on a Nicolet-Nexus 670 infrared spectrometer. The nitrogen adsorption isotherm was measured at 77 K with an ASAP 2020 Accelerated Surface Area and Porosimetry System (Micromeritics, Norcross, GA) and the specific surface area, pore volume and mean pore diameter are determined by the Brunauer–Emmett–Teller (BET) and Barrett–Joyner–Halenda (BJH) method.

Electrochemical testing

Firstly, the active material, Super-P carbon black (conducting additive) and polyvinylidene fluoride (PVDF, binder), with a weight ratio of 80:10:10, were homogenously mixed in N-methyl-2-pyrrolidone (NMP, solvent) for at least 24 h to produce slurry. Secondly, the obtained slurry was coated onto a piece of copper foil using a doctor blading method, dried at 120 °C in vacuum oven for 12 h, and then punched into round plates (diameter of 14.0 mm) as the anode electrodes. Finally, the as-prepared anode, a Celgard 2325 separator (diameter of 19.0 mm), a pure lithium counter electrode, electrolyte of 1M LiPF_6 in EC-DEC-EMC (1:1:1 vol %), and the other components of the coin-type cell were assembled into a coin cell (CR2032) in an argon filled glove box with oxygen and water less than 0.1 ppm. The assembled coin-type cells were aged for at least 12 h before electrochemical test. Galvanostatic charge-discharge cycles were performed using a LAND 2001A battery test system in the voltage range of 0.001–3 V. Cyclic voltammetry (CV) was performed using an electrochemical workstation (AUTOLAB PGSTAT302N) between the voltage range of 0.001–3 V at a scan rate of 0.5 mV s^{-1} . Electrochemical impedance spectroscopy (ESI) measurements tests were also carried out on an electrochemical workstation (AUTOLAB PGSTAT302N) with the frequency range of 10^4 Hz to 10^{-2} Hz.

Acknowledgements

Authors are grateful for the funding supported by “National Key Basic Research Program of China (2013CB921800)”, large instruments Open Foundation of East China Normal University, “the support from the Shanghai Committee of Science and Technology (11JC1403600)” and “National Natural Science Foundation of China (21103050, 21373086)”.

Notes and references

- ^aShanghai Key Laboratory of Magnetic Resonance, Department of Physics, Engineering Research Center for Nanophotonics & Advanced Instrument, Ministry of Education, East China Normal University, Shanghai 200062, China. E-mail: bwhu@phy.ecnu.edu.cn
- † Electronic Supplementary Information (ESI) available: XRD pattern and TEM images of the as-prepared Co-MOF-71 (Fig. S1), FT-IR spectrum of MOF-71@450N (Fig. S2), TG curves of MOF-71@300N and MOF-71@450N under air atmosphere (Fig. S3 and S4), TEM and HRTEM of MOF-71@450N (Fig. S5), charge/discharge voltage profiles of MOF-71@450N anode at a current density of 200 mA g⁻¹ (Fig. S6), Coulombic efficiencies of MOF-71@450N anode when cycling at 200 mA g⁻¹ (Fig. S7), Nyquist plots for MOF-71@300N and MOF-71@450N at 30th cycles (Fig. S8), charge/discharge profiles in the first cycle of MOF-71@300N anode at different current rates (Fig. S9), ex-situ TEM images of MOF-71@300N electrodes taken from the fully charged states after 30 cycles (Fig. S10), surface areas, pore volumes and mean pore diameters of MOF-71@300N and MOF-71@450N (Table S1), cycling performance of Co₃O₄ as anode material under similar conditions in recent papers (Table S2). See DOI: 10.1039/b000000x/
- 1 M. Armand and J. -M. Tarascon, *Nature*, 2008, **451**, 652–657.
 - 2 J. -M. Tarascon, *Nat. chem*, 2010, **2**, 520.
 - 3 F. Cheng, J. Liang, Z. Tao and J. Chen, *Adv. Mater.*, 2011, **23**, 1695–1725.
 - 4 P. Poizot, S. Laruelle, S. Grugeon, L. Dupon, J. M. Tarascon, *Nature*, 2000, **407**, 496–499.
 - 5 J. Cabana, L. Monconduit, D. Larcher, M. R. Palacín, *Adv. Mater.*, 2010, **22**, 170–192.
 - 6 X. Dong, H. Xu, X. Wang, Y. Huang, M. Chan-Park, H. Zhang, L. Wang, W. Huang and P. Chen, *ACS Nano*, 2012, **6**, 3206–3213.
 - 7 L. Tian, H. Zou, J. Fu, X. Yang, Y. Wang, H. Guo, X. Fu, C. Liang, M. Wu, P. Shen, Q. Gao, *Adv. Funct. Mater.*, 2010, **20**, 617–623.
 - 8 D. Ge, H. Geng, J. Wang, J. Zheng, Y. Pan, X. Cao, H. Gu, *Nanoscale*, 2014, **6**, 9689–9694.
 - 9 X. Chen, W. Wei, W. Lv, F. Su, Y. He, B. Li, F. Kang and Q. Yang, *Chem. Commun.*, 2012, **48**, 5904–5906.
 - 10 Y. Li, B. Tan, Y. Wu, *Nano Lett.*, 2008, **8**, 265–270.
 - 11 X. W. Lou, D. Deng, J. Y. Lee, J. Feng, L. A. Archer, *Adv. Mater.*, 2008, **20**, 258–262.
 - 12 C. Li, X. Yin, L. Chen, Q. Li, T. Wang, *Chem. Eur. J.*, 2010, **16**, 5215–5221.
 - 13 Y. Wang, H. Xia, L. Lu, J. Lin, *ACS Nano*, 2010, **4**, 1425–1432.
 - 14 N. Du, H. Zhang, B. Chen, J. Wu, X. Ma, Z. Liu, Y. Zhang, D. Yang, X. Huang, J. Tu, *Adv. Mater.*, 2007, **19**, 4505–4509.
 - 15 F. Zhan, B. Geng, Y. Guo, *Chem. Eur. J.*, 2009, **15**, 6169–6174.
 - 16 L. Wang, B. Liu, S. Ran, H. Huang, X. Wang, B. Liang, D. Chen and G. Shen, *J. Mater. Chem.*, 2012, **22**, 23541–23546.
 - 17 X. Wang, X. Wu, Y. Guo, Y. Zhong, X. Cao, Y. Ma, J. Yao, *Adv. Funct. Mater.*, 2010, **20**, 1680–1686.
 - 18 J. L. Rowsell, O. M. Yaghi, *Angew. Chem. Int. Ed.*, 2005, **44**, 4670–4679.
 - 19 J. K. Clegg, S. S. Iremonger, M. J. Hayter, P. D. Southon, R. B. Macquart, M. B. Duriska, P. Jensen, P. Turner, K. A. Jolliffe, C. J. Kepert, G. V. Meehan, L. F. Lindoy, *Angew. Chem. Int. Ed.*, 2010, **49**, 1075.
 - 20 S. -H. Cho, B. Ma, S. B. T. Nguyen, J. T. Hupp, T. E. Albrecht-Schmitt, *Chem. Commun.*, 2006, **24**, 2563–2565.
 - 21 M. Sadakiyo, T. Yamada, H. Kitagawa, *J. Am. Chem. Soc.*, 2009, **131**, 9906–9907.
 - 22 J. M. Taylor, R. K. Mah, I. L. Moudrakovski, C. I. Ratcliffe, R. Vaidhyanathan, and G. K. H. Shimizu, *J. Am. Chem. Soc.*, 2010, **132**, 14055–14057.
 - 23 H. Wu, Y. S. Chua, V. Krungleviciute, M. Tyagi, P. Chen, T. Yildirim and W. Zhou, *J. Am. Chem. Soc.*, 2013, **135**, 10525–10532.
 - 24 V. Finsy, H. Verelst, L. Alaerts, D. D. Vos, P. A. Jacobs, G. V. Baron and J. F. M. Denayer, *J. Am. Chem. Soc.*, 2008, **130**, 7110–7118.
 - 25 J. S. Seo, D. Whang, H. Lee, S. I. Jun, J. Oh, Y. J. Jeon and K. Kim, *Nature*, 2000, **404**, 982–986.
 - 26 S. Takaishi, M. Hosoda, T. Kajiwarra, H. Miyasaka, M. Yamashita, Y. Nakanishi, Y. Kitagawa, K. Yamaguchi, A. Kobayashi, H. Kitagawa, *Inorg. Chem.*, 2009, **48**, 9048–9050.
 - 27 S. R. Kim, K. W. Dawson, B. S. Gelfand, J. M. Taylor, and G. K. H. Shimizu, *J. Am. Chem. Soc.*, 2013, **135**, 963–966.
 - 28 Y. Han, P. Qi, S. Li, X. Feng, J. Zhou, H. Li, S. Su, X. Li and B. Wang, *Chem. Commun.*, 2014, **50**, 8057.
 - 29 X. Xu, R. Cao, S. Jeong and J. Cho, *Nano Lett.*, 2012, **12**, 4988–4991.
 - 30 R. Wu, X. Qian, F. Yu, H. Liu, K. Zhou, J. Wei and Y. Huang, *J. Mater. Chem. A*, 2013, **1**, 11126.
 - 31 L. Hu, Y. Huang, F. Zhang and Q. Chen, *Nanoscale*, 2013, **5**, 4186.
 - 32 L. Zhang, H. Wu, S. Madhavi, H. Hng and X. Lou, *J. Am. Chem. Soc.*, 2012, **134**, 17388–17391.
 - 33 J. Zhao, F. Wang, P. Su, M. Li, J. Chen, Q. Yang and C. Li, *J. Mater. Chem.*, 2012, **22**, 13328.
 - 34 J. Shao, Z. Wan, H. Liu, H. Zheng, T. Gao, M. Shen, Q. Qu and H. Zheng, *J. Mater. Chem. A*, 2014, **2**, 12194.
 - 35 N. L. Rosi, J. Kim, M. Eddaoudi, B. Chen, M. O’Keeffe, O. M. Yaghi, *J. Am. Chem. Soc.*, 2005, **127**, 1504–1518.
 - 36 D. O. Miles, D. Jiang, A. D. Burrows, J. E. Halls, F. Marken, *Electrochem Commun.*, 2012, **2**, 9–13.
 - 37 W. Hao, S. Chen, Y. Cai, L. Zhang, Z. Li, S. Zhang, *J. Mater. Chem. A*, 2014, **2**, 13801–13804.
 - 38 B. Liu, X. Zhang, H. Shioyama, T. Mukai, T. Sakai, Q. Xu, *J. Power. Sources.*, 2010, **195**, 857–861.
 - 39 Q. Su, J. Zhang, Y. Wu and G. Du, *Nano Energy*, 2014, **9**, 264–272.
 - 40 R. Wang, C. Xu, J. Sun, Y. Liu, L. Cao and C. Lin, *Nanoscale*, 2013, **5**, 6960.
 - 41 R. Sahay, P. S. Kumar, V. Aravindan, J. Sundaramurthy, W. C. Ling, S. G. Mhaisalkar, S. Ramakrishna and S. Madhavi, *J. Phys. Chem. C*, 2012, **116**, 18087–18092.
 - 42 J. Wang, N. Yang, H. Tang, Z. Dong, Q. Jin, M. Wang, D. Kisailus, H. Zhao, Z. Tang and D. Wang, *Angew. Chem. Int. Ed.*, 2013, **52**, 6417–6420.
 - 43 X. -L. Huang, R. -Z. Wang, D. Xu, Z. -L. Wang, H. -G. Wang, J. -J. Xu, Z. Wu, Q. -C. Liu, Y. Zhang and X. -B. Zhang, *Adv. Funct. Mater.*, 2013, **23**, 4345.
 - 44 X. Wang, X. Li, X. Sun, F. Li, Q. Liu, Q. Wang and D. He, *J. Mater. Chem.*, 2011, **21**, 3571–3573.
 - 45 H. W. Shim, Y. H. Jin, S. D. Seo, S. H. Lee, D. W. Kim, *ACS Nano*, 2011, **5**, 443–449.
 - 46 Y. Wang, H. Zhang, J. Wei, C. Wong, J. Lin and A. Borgna, *Energy. Environ. Sci.*, 2011, **4**, 1845–1854.
 - 47 R. Wu, X. Qian, X. Rui, H. Liu, B. Yadian, K. Zhou, J. Wei, Q. Yan, X. Q. Feng, Y. Long, L. Wang and Y. Huang, *Small*, 2014, **10**, 1932–1938.
 - 48 R. Ma, Y. Dong, L. Xi, S. Yang, Z. Lu and C. Chung, *ACS Appl. Mater. Interfaces*, 2013, **5**, 892–897.